Compton profile of VO_2 across the metal-insulator transition: Evidence of a non-Fermi liquid metal

Ilkka Kylänpää,[1,2,*] Ye Luo,[3] Olle Heinonen,[4,5] Paul R. C. Kent,[6,7] and Jaron T. Krogel[1]

[1]*Materials Science and Technology Division, Oak Ridge National Laboratory, Oak Ridge, Tennessee 37831, USA*
[2]*Computational Physics Laboratory, Tampere University, P.O. Box 692, 33014 Tampere, Finland*
[3]*Computational Science Division, Argonne National Laboratory, Lemont, Illinois 60439, USA*
[4]*Materials Science Division, Argonne National Laboratory, Lemont, Illinois 60439, USA*
[5]*Center for Hierarchical Material Design, Northwestern-Argonne Institute for Science and Engineering, Northwestern University, Evanston, Illinois 60208, USA*
[6]*Center for Nanophase Materials Sciences, Oak Ridge National Laboratory, Oak Ridge, Tennessee 37831, USA*
[7]*Computational Sciences and Engineering Division, Oak Ridge National Laboratory, Oak Ridge, Tennessee 37831, USA*

(Received 18 May 2018; published 26 February 2019)

Many-body diffusion Monte Carlo is used to obtain the first-principles momentum distribution and Compton profile of vanadium dioxide. Our results for the Compton profile are in good agreement with the experimental values, and we show that good qualitative agreement in the scaled Compton profile difference across the monoclinic to rutile phase transition depends on an accurate description of electron correlation. The electron momentum distribution enables new insights into the metal-insulator phase transition. For example, the probability for electron scattering in the proximity of the Fermi surface (forward scattering) is suppressed in the vanadium chain direction (rutile c axis) but enhanced in perpendicular directions. However, along the c axis we observe an increase at $\sim 2k_F$ in the momentum distribution, which is characteristic for Friedel oscillations (backscattering). Our analysis of the momentum distribution supports experimentally observed anisotropies and provides an explanation for the anomalously low electronic thermal conductivity observed recently in the metallic phase [S. Lee *et al.*, Science **355**, 371 (2017)]. Moreover, our results indicate non-Fermi liquid behavior as well as quasi-one-dimensional Friedel oscillations in the metallic rutile phase, which is reminiscent of a Tomanaga-Luttinger liquid with impurities.

DOI: 10.1103/PhysRevB.99.075154

I. INTRODUCTION

Vanadium dioxide (VO_2) is an amphoteric oxide with functional properties suitable for various solid-state applications, including glass optics, ceramic applications, data storage, and fast optical shutters [1]. It has also become known as a prototypical strongly correlated electron material that challenges theoretical and computational modeling [2–6]. For example, despite its success with various materials, density functional theory (DFT) has not been able to adequately capture the electronic and magnetic structures of VO_2 [7]. This is in part due to electronic correlations that DFT does not capture accurately [8]. In 2015 Zheng and Wagner [9] demonstrated the need for a higher-accuracy many-body approach, i.e., quantum Monte Carlo (QMC), to correctly describe the electronic and magnetic structures of VO_2. Accurate spectral properties, however, have successfully been obtained by beyond DFT approaches such as dynamical mean-field theory (DMFT) [10–12] and many-body perturbation theory (GW) [13,14].

The wealth of interest in VO_2 stems from its rich phase diagram with desirable properties controllable, e.g., by temperature, pressure, and doping [15–22]. Here we focus on the thermally induced metal to insulator transition (MIT) from the insulating monoclinic phase ($M1$, $T < T_c$) into a metallic rutile phase (R, $T > T_c$) [23–25]. This tunable MIT is accompanied by a change in the underlying crystal lattice structure, which at ambient pressure occurs at $T_c \approx 341$ K for pure unstrained VO_2. This transition was very recently studied with Compton profile measurements [26], which revealed poor correspondence between the experiments and theoretical DFT results. Moreover, the high-temperature metallic phase was observed recently to exhibit a peculiar non-Fermi liquid character and anomalously low electronic thermal conductivity [15]. Earlier experiments had already shown a strong anisotropy in the metallic phase, with the conduction along the rutile c axis suppressed compared to the perpendicular directions [27]. We use the momentum distribution $n(k)$ and Compton profile $J(q)$ to address the transition and the nature of the metallic R phase: is it a normal Fermi liquid, and what signatures do $n(k)$ and $J(q)$ reveal?

Both the momentum distribution and Compton profile are powerful probes for understanding the ground-state properties of materials. The momentum distribution of the electrons can be experimentally studied by scattering methods such as Compton scattering, positron annihilation, the $(e, 2e)$ process, and high-energy electron scattering [28–31]. In general, the differential cross sections can be related to the momentum distribution. For Compton scattering this requires an assumption that the transferred energy and momentum are high

*ilkka.kylanpaa@tuni.fi

compared to those characteristic of the ground-state properties and collective behavior. This assumption results in the "impulse approximation" (IA) in which, e.g., the Compton profile and the dynamical structure factor are proportional to the projection of $n(k)$ onto a scattering vector [32,33]. Within the IA the directional Compton profile in the z direction is given as

$$J(q) = \iint n(k_x, k_y, k_z = q) dk_x dk_y. \quad (1)$$

The IA is especially appropriate for x-ray Compton scattering from electronic systems [30,32], and thus, it is capable of providing a unique perspective for understanding the electronic structure of materials, the properties of the bulk, in particular.

In normal Fermi liquids, the electron momentum distribution has a discontinuity at the Fermi momentum k_F. In three-dimensional systems this discontinuity defines the shape of the Fermi surface, which is also related to the screening properties of the electrons [34]. The magnitude of the discontinuity at the Fermi surface, on the other hand, quantifies the strength of a quasiparticle excitation and is called the renormalization factor Z [35,36]. For strongly coupled systems Z tends to zero as the coupling strength increases, which can be used as a measure of electron correlations. In the case of superfluidity or superconducting behavior the Fermi surface actually disappears, and the discontinuity is absent also in some semimetals [32]. Interestingly, even the smallest amount of interaction will destroy the discontinuity in $n(k)$ in one-dimensional (1D) chains according to the Tomanaga-Luttinger theory [37–39]. Broadening of the sharp drop at k_F is also associated with the opening of a band gap [40]. To this end, the momentum distribution provides knowledge complementary to, and possibly even more informative than, other characterizations of many-body systems.

Here we will first motivate the use of our first-principles approach, i.e., QMC, and discuss computational details. Second, we will show that our QMC results are in excellent *qualitative* agreement with recent experimental data [26] on the scaled Compton profile difference across the MIT. Third, we will address the origin of the *quantitative* discrepancy between theory and experiment. Then we will consider the subtle details of the momentum distribution across the MIT and in individual phases (the R phase in particular) and explain possible implications of the underlying physics. This analysis is further tied to insights obtained from postprocessed electron densities from Ref. [8].

II. METHODS AND COMPUTATIONAL DETAILS

Using continuum diffusion Monte Carlo (DMC) [41–43], we are able to obtain the momentum distribution function from first principles. This is accomplished by evaluation of the expectation value

$$n(\mathbf{k}) = \Omega^{-1} \sum_{j=1}^{N} \left\langle \int d\mathbf{s}_j \frac{\Psi(R + \mathbf{s}_j)}{\Psi(R)} e^{-i\mathbf{k}\cdot\mathbf{s}_j} \right\rangle_{|\Psi(R)|^2}, \quad (2)$$

where Ω is the volume containing N electrons, R includes the coordinates of all the electrons, and $\mathbf{s}_j$ is a displacement vector acting on the jth electron. The DMC approach is known for its accuracy in solving ground-state electronic structure properties for both molecular and solid-state systems from first principles [9,42,44–46]. In particular, DMC straightforwardly and accurately includes electron correlations [47–49]. Importantly, in recent years it has been demonstrated that the challenges introduced by electron correlation and the description of $3d$ orbitals of transition-metal oxides are overcome by DMC [49–64]. Therefore, QMC is regarded as an excellent computational tool for validating and predicting material properties. Use of QMC in periodic supercells results in finite-size effects, but unexpectedly, we find that these are small for $n(k)$ in VO_2, which differs from past experience with the homogeneous electron gas [36,65].

Crystal structures for the $M1$ [66] and R [67] phases were obtained from the Inorganic Crystal Structure Database [68]. All calculations were performed with the experimental lattice constants. In both phases, the vanadium atoms are arranged in quasi-1D chains, and as in Ref. [9], an antiferromagnetic ordering was imposed by fixing alternating up and down spin moments along the chains. More details on the experimental lattice vectors and atomic coordinates of the $M1$ and R crystal structures are given below regarding our DFT and QMC calculations [69].

A. Density functional theory

Our DFT calculations were performed in the antiferromagnetic (AFM) magnetic primitive cell of VO_2 (four VO_2 formula units for $M1$ and R). We used experimental crystal structures [66,67] from the Inorganic Crystal Structure Database (ICSD). See Table I for information on the axes and atomic positions. In Table I we use V1 and V2 when referring to the different magnetic orientations of the vanadium atoms (spin up and spin down, respectively). We used plane-wave energy cutoffs of 350 Ry with $12 \times 12 \times 24$ and $24 \times 12 \times 12$ k-space grids for the R phase and $M1$ phase, respectively. The DFT calculations were performed with QUANTUM ESPRESSO [70] using hard norm-conserving pseudopotentials as in our earlier study [8].

B. Quantum Monte Carlo

The quantum Monte Carlo simulations were carried out with QMCPACK [43,71] in a supercell containing 16 VO_2 formula units, that is, a 48-atom supercell. The experimental crystal structures used in DFT calculations were tiled to give the supercells described in Table II. For faster convergence to thermodynamic limit, we used twist-averaged boundary conditions [72] with a $4 \times 4 \times 4$ supercell twist angle grid instead of purely periodic boundary conditions. Twist-averaging also results in better resolution of the momentum distribution. In order to estimate the finite-size effects on the momentum distribution we performed additional simulations for the R phase for 72- and 96-atom supercells. We find that the momentum distribution is well converged already with our 48-atom supercell, as can be seen in Fig. 1, where we show the difference between the larger supercells and the 48-atom cell along the rutile c axis. The differences show no consistency to increase or decrease, and the magnitude is also small, roughly zero within two standard deviations.

TABLE I. Primitive-cell axes and atomic positions (in Å) used in density functional theory calculations. These are experimental structures: for the $M1$ phase we use ICSD collection code entry 34033, and for the R phase we use ICSD entry 1504. Vanadium sites with up (down) magnetic moment are labeled V1 (V2).

	$M1$ phase ($P2_1/c$)			R phase ($P4_2/mnm$)		
	x	y	z	x	y	z
a	5.752000000	0.000000000	0.000000000	4.554600000	0.000000000	0.000000000
b	0.000000000	4.537800000	0.000000000	0.000000000	4.554600000	0.000000000
c	−2.903573350	0.000000000	4.532170350	0.000000000	0.000000000	5.705600000
V1	1.300602890	4.442233932	0.119921229	0.000000000	0.000000000	0.000000000
V2	1.547823771	0.095566070	4.412249122	0.000000000	0.000000000	2.852799999
V1	−0.151183780	2.364466069	2.386006401	2.277299999	2.277299999	1.426399997
V2	2.999610442	2.173333934	2.146163949	2.277299999	2.277299999	4.279200001
O	0.005176999	0.961559820	0.945410729	1.366835461	1.366835461	0.000000000
O	2.843249652	3.576240182	3.586759611	3.187764536	3.187764536	0.000000000
O	−1.446609671	1.307340179	3.211495912	3.644135460	0.910464538	1.426399997
O	4.295036333	3.230459824	1.320674439	0.910464538	3.644135460	1.426399997
O	1.436088279	3.188258280	1.354212500	1.366835461	1.366835461	2.852799999
O	1.412338372	1.349541722	3.177957851	3.187764536	3.187764536	2.852799999
O	−0.015698391	3.618441721	3.620297683	3.644135460	0.910464538	4.279200001
O	2.864125042	0.919358281	0.911872668	0.910464538	3.644135460	4.279200001

The trial wave function Ψ_T used is of the standard Slater-Jastrow [73,74] type:

$$\Psi_T = \det\{\psi_\uparrow\}\det\{\psi_\downarrow\}e^J. \quad (3)$$

The purpose of the trial wave function is to guide the simulation both more accurately and more rapidly to the ground state. A trial wave function with a better nodal surface, arising from the sets of orbitals above, leads to a more accurate DMC result. A trial wave function with a better Jastrow factor improves the time step and pseudopotential localization approximations made in DMC and also reduces the statistical variance, making the calculations more efficient. Since a good trial wave function is important in improving the approximations made in DMC, we describe in more detail below how we obtained an optimal wave function within the Slater-Jastrow ansatz.

The product of spin-up and spin-down determinants of spatial orbitals arises from a single determinant of spin orbitals after fixing the electron spins, while the overall state is a spin-unrestricted antiferromagnet [51]. The determinants are composed of single-particle orbitals taken from spin-unrestricted local-density approximation (LDA) + U (via QUANTUM ESPRESSO), in which the correct magnetic structure was imposed by initializing the magnetic moments in an antiferromagnetic configuration along the V-V chains. Convergence to the AFM state was further confirmed after the self-consistent density functional theory calculations by analysis of the magnetic structure and spin-resolved Löwdin charges.

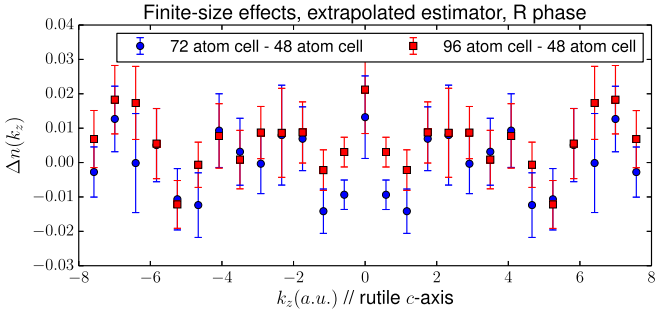

FIG. 1. Finite-size effects on the momentum distribution considered as the difference between 72-atom and 48-atom as well as 96-atom and 48-atom supercells.

In the Jastrow factor e^J we include terms up to two-body (electron-electron) correlation functions, i.e.,

$$J = J_1 + J_2 = \sum_{I,i} u_1(|r_i - R_I|) + \sum_{i<j} u_2(|r_i - r_j|), \quad (4)$$

where r_i and R_I refer to electron and ion coordinates, respectively. The u_1 and u_2 correlation functions depend, as appropriate, on both the ionic and spin species involved. The functions u_1 and u_2 are parameterized in terms of radial B splines [75].

The Jastrow parameters were optimized by making use of the variational principle as applied to the total energy and the energy variance. The optimization was performed by minimizing a cost function containing a 95:5 ratio of energy and variance with the linear method [76], which results in a good balance between improvements in DMC pseudopotential localization approximation [77–79] and the resulting variance of the local energy [80]. We optimize the Jastrow part only with variational Monte Carlo (VMC), which improves the description of particle-particle correlations but does not modify the nodal surface. The orbitals are instead optimized directly with DMC, although within the restricted variational freedom afforded by LDA+U.

In DMC the operator $\exp[-\tau(\hat{H} - E_T)]$ is used to project out the lowest eigenstate that has nonzero overlap with the chosen fixed-node/trial wave function [42], where $\hat{H}$ is the many-body Hamiltonian and E_T is an estimate of the ground-state energy, which is updated throughout the simulation.

TABLE II. Supercell axes and atomic positions (in Å) used in quantum Monte Carlo simulations.

	*M*1 phase			*R* phase		
	x	*y*	*z*	*x*	*y*	*z*
a	11.50400000	0.00000000	0.00000000	4.55460000	−4.55460000	0.00000000
b	2.90357335	4.53780000	−4.53217035	4.55460000	4.55460000	0.00000000
c	−2.90357335	4.53780000	4.53217035	0.00000000	0.00000000	11.41120000
V1	1.30060289	4.44223393	0.11992123	0.00000000	0.00000000	0.00000000
V2	4.45139712	4.63336607	−0.11992123	0.00000000	0.00000000	2.85280000
V1	2.75238957	6.90226607	−2.14616395	4.55460000	0.00000000	0.00000000
V2	2.99961044	2.17333393	2.14616395	4.55460000	0.00000000	2.85280000
V1	7.05260289	4.44223393	0.11992123	0.00000000	0.00000000	5.70560000
V2	10.20339712	4.63336607	−0.11992123	0.00000000	0.00000000	8.55840000
V1	8.50438957	6.90226607	−2.14616395	4.55460000	0.00000000	5.70560000
V2	8.75161044	2.17333393	2.14616395	4.55460000	0.00000000	8.55840000
V1	4.20417624	4.44223393	−4.41224912	2.27730000	2.27730000	1.42640000
V2	1.54782377	4.63336607	4.41224912	2.27730000	2.27730000	4.27920000
V1	2.75238957	2.36446607	−2.14616395	2.27730000	−2.27730000	1.42640000
V2	2.99961044	6.71113393	2.14616395	2.27730000	−2.27730000	4.27920000
V1	9.95617624	4.44223393	−4.41224912	2.27730000	2.27730000	7.13200000
V2	7.29982377	4.63336607	4.41224912	2.27730000	2.27730000	9.98480000
V1	8.50438957	2.36446607	−2.14616395	2.27730000	−2.27730000	7.13200000
V2	8.75161044	6.71113393	2.14616395	2.27730000	−2.27730000	9.98480000
O	0.00517700	0.96155982	0.94541073	1.36683546	1.36683546	0.00000000
O	5.74682300	8.11404018	−0.94541074	3.18776454	3.18776454	0.00000000
O	1.45696368	5.84514018	−1.32067444	3.64413546	0.91046454	1.42640000
O	4.29503633	3.23045982	1.32067444	5.46506454	−0.91046454	1.42640000
O	1.43608828	3.18825828	1.35421250	1.36683546	1.36683546	2.85280000
O	4.31591172	5.88734172	−1.35421250	3.18776454	3.18776454	2.85280000
O	2.88787496	8.15624172	−0.91187267	3.64413546	0.91046454	4.27920000
O	2.86412504	0.91935828	0.91187267	5.46506454	−0.91046454	4.27920000
O	5.75717700	0.96155982	0.94541073	5.92143546	1.36683546	0.00000000
O	11.49882300	8.11404018	−0.94541074	3.18776454	−1.36683546	0.00000000
O	7.20896368	5.84514018	−1.32067444	3.64413546	−3.64413546	1.42640000
O	10.04703633	3.23045982	1.32067444	0.91046454	−0.91046454	1.42640000
O	7.18808828	3.18825828	1.35421250	5.92143546	1.36683546	2.85280000
O	10.06791172	5.88734172	−1.35421250	3.18776454	−1.36683546	2.85280000
O	8.63987496	8.15624172	−0.91187267	3.64413546	−3.64413546	4.27920000
O	8.61612504	0.91935828	0.91187267	0.91046454	−0.91046454	4.27920000
O	0.00517700	5.49935982	0.94541073	1.36683546	1.36683546	5.70560000
O	5.74682300	3.57624018	−0.94541074	3.18776454	3.18776454	5.70560000
O	−1.44660967	5.84514018	3.21149591	3.64413546	0.91046454	7.13200000
O	7.19860968	3.23045982	−3.21149591	5.46506454	−0.91046454	7.13200000
O	4.33966163	3.18825828	−3.17795785	1.36683546	1.36683546	8.55840000
O	1.41233837	5.88734172	3.17795785	3.18776454	3.18776454	8.55840000
O	2.88787496	3.61844172	−0.91187267	3.64413546	0.91046454	9.98480000
O	2.86412504	5.45715828	0.91187267	5.46506454	−0.91046454	9.98480000
O	5.75717700	5.49935982	0.94541073	5.92143546	1.36683546	5.70560000
O	11.49882300	3.57624018	−0.94541074	3.18776454	−1.36683546	5.70560000
O	4.30539033	5.84514018	3.21149591	3.64413546	−3.64413546	7.13200000
O	12.95060968	3.23045982	−3.21149591	0.91046454	−0.91046454	7.13200000
O	10.09166163	3.18825828	−3.17795785	5.92143546	1.36683546	8.55840000
O	7.16433837	5.88734172	3.17795785	3.18776454	−1.36683546	8.55840000
O	8.63987496	3.61844172	−0.91187267	3.64413546	−3.64413546	9.98480000
O	8.61612504	5.45715828	0.91187267	0.91046454	−0.91046454	9.98480000

In our earlier work [8] the DMC fixed-node/phase error [47,81,82] was minimized by using the Hubbard U value as a variational parameter optimized directly in DMC, with $U = 3.5$ eV yielding the lowest energy. In production runs, the DMC time step was set to 0.005 Ha^{-1}, resulting in an acceptance ratio greater than 99.6%. Nonlocal pseudopotentials were handled in the DMC projector within the variational T-moves scheme [79,83].

Since DMC provides a "mixed" estimate of the momentum distribution (a mixture between the fixed-node estimate and the VMC one), we have corrected the mixed estimates by extrapolation to obtain "pure" estimates of the momentum distribution, reflecting the fixed-node wave function Φ alone. This is a general property of the DMC method for operators that do not commute with the Hamiltonian. In order to obtain pure estimates of the momentum distribution $n(k)$, we used the extrapolation formula [42]

$$n_{\text{extrap}} = 2n_{\text{DMC,mixed}} - n_{\text{VMC}} + O((\Phi - \Psi_T)^2). \quad (5)$$

C. Momentum distribution and Compton profile

Momentum distribution $n(\mathbf{k})$ is obtained by taking the Fourier transform of the one-body density matrix:

$$\begin{aligned} n(\mathbf{k}) &= \frac{N}{\Omega}\int d\mathbf{R}d\mathbf{r}_1'\, e^{i(\mathbf{r}_1-\mathbf{r}_1')\cdot\mathbf{k}}\rho(\mathbf{r}_1,\ldots,\mathbf{r}_N,\mathbf{r}_1',\ldots,\mathbf{r}_N) \\ &= \frac{N}{\Omega}\int d\mathbf{s}\, e^{-i\mathbf{k}\cdot\mathbf{s}}n(\mathbf{s}), \end{aligned}$$

where N is the number of electrons, $\mathbf{R} = \{\mathbf{r}_1,\ldots,\mathbf{r}_N\}$, $\mathbf{s} = \mathbf{r}_1' - \mathbf{r}_1$, and

$$n(\mathbf{s}) = \int d\mathbf{R}\ \rho(\mathbf{r}_1,\ldots,\mathbf{r}_N,\mathbf{r}_1+\mathbf{s},\ldots,\mathbf{r}_N).$$

In VMC and DMC

$$\begin{aligned} n(\mathbf{s}) &= \int d\mathbf{R}\ \Psi^*(\mathbf{r}_1,\ldots,\mathbf{r}_N)\Psi(\mathbf{r}_1+\mathbf{s},\ldots,\mathbf{r}_N) \\ &= \int d\mathbf{R}\ |\Psi(R)|^2\frac{\Psi(R')}{\Psi(R)}, \end{aligned}$$

which gives us

$$n(\mathbf{k}) = \int d\mathbf{R}\ |\Psi(R)|^2\frac{N}{\Omega}\int d\mathbf{s}\frac{\Psi(R')}{\Psi(R)}e^{-i\mathbf{k}\cdot\mathbf{s}}.$$

In practice, the above will be estimated through

$$n(\mathbf{k}) = \left\langle \frac{N}{\Omega}\frac{1}{N_s}\sum_{j=1}^{N_s}\frac{\Psi(R')}{\Psi(R)}e^{-i\mathbf{k}\cdot\mathbf{s}_j}\right\rangle_{|\Psi(R)|^2}, \quad (6)$$

where N_s refers to the number of samples used in the Monte Carlo integral for $\int d\mathbf{s}$. Notice that the momentum distribution normalizes to the number of electrons,

$$\sum_{\mathbf{k}} n(\mathbf{k}) = N = \frac{\Omega}{(2\pi)^d}\int d\mathbf{k}\ n(\mathbf{k}) = \int d\mathbf{k}\ \widetilde{n}(\mathbf{k}), \quad (7)$$

in which a finite system and a system at the thermodynamic limit are described by summation and integration, respectively, and $\widetilde{n}(\mathbf{k}) = (2\pi)^{-d}\Omega n(\mathbf{k})$.

The Compton profile is obtained as an integral of the momentum distribution [30]. For example, the directional Compton profile in the z direction is given as

$$J(q) = \int dk_x dk_y\ \widetilde{n}(k_x,k_y,k_z=q). \quad (8)$$

In the spherically symmetrized (or isotropic) case we have

$$\begin{aligned} J(q) &= \frac{1}{2}\int_{|q|}^{\infty} dk\ \frac{1}{k}I(k) \\ &= \frac{1}{2}\int_{|q|}^{\infty} dk\ \frac{1}{k}4\pi k^2\widetilde{n}(k) \\ &= 2\pi\int_{|q|}^{\infty} dk\ k\widetilde{n}(k), \end{aligned} \quad (9)$$

with $I(k) = 4\pi k^2\widetilde{n}(k)$. Also the Compton profile normalizes to the number of electrons, i.e.,

$$\int_{-\infty}^{\infty} dqJ(q) = N. \quad (10)$$

In practice with periodic simulations we need to resort to a finite number of k points in which we describe the momentum distribution. This introduces a cutoff k_c into our k grid. Let's consider this in the case of a spherically symmetric (or angular-averaged) momentum distribution and the related Compton profile. According to Eq. (7), we can write

$$\begin{aligned} N &= \int d\mathbf{k}\ \widetilde{n}(\mathbf{k}) \\ &= \int_0^{k_c} dk\ 4\pi k^2\widetilde{n}(k) + \Delta N. \end{aligned} \quad (11)$$

Considering large enough k_c we can approximate the tail by a decaying function such as $A\exp(-Bk)/k$, and thus,

$$\begin{aligned} \Delta N &= \int_{k_c}^{\infty} dk\ 4\pi k^2\widetilde{n}(k) \\ &\approx \int_{k_c}^{\infty} dk\ 4\pi kAe^{-Bk} \\ &= \frac{4\pi A}{B^2}[1+Bk_c]e^{-Bk_c}. \end{aligned} \quad (12)$$

Therefore, in optimizing the coefficients for the tail it is also possible to use the accuracy in ΔN as a constraint in addition to the few points at the tail.

For the "isotropic" Compton profile this yields

$$J(q) = 2\pi\int_{|q|}^{\infty} dk\ k\widetilde{n}(k) = 2\pi\int_{|q|}^{k_c} dk\ k\widetilde{n}(k) + \Delta J, \quad (13)$$

where

$$\Delta J = 2\pi\int_{k_c}^{\infty} dk\ k\widetilde{n}(k) \approx \frac{2\pi A}{B}e^{-Bk_c}. \quad (14)$$

Notice that for $q \geqslant k_c$ the tail of the isotropic Compton profile can be approximated by Eq. (14). This can be used in the calculation of the norm of the Compton profile in the range $(-\infty,\infty)$:

$$N = \int_{-\infty}^{\infty} dqJ(q) = 2\int_0^{q_c} J(q) + 2\Delta N, \quad (15)$$

where the "correction term" ΔN to the norm is given by

$$\Delta N = \int_{k_c}^{\infty} dq\Delta J \approx \frac{2\pi A}{B^2}e^{-Bk_c}. \quad (16)$$

Another aspect arising from periodic simulations might be harder to notice, but it can be dealt with by converging the trial wave function with a set of k points that includes the desired k grid. That is, already at the DFT level the self-consistent-field (SCF) calculation should include the k points that will be used in the non-self-consistent-field (NSCF) calculation for the trial wave function. Failing to do this would lead to some sort of "interpolation" between the k points of the SCF calculation, which can introduce subtle, but noticeable, inconsistencies, at least in the momentum distribution. In the Compton profile these small inconsistencies would, however, be suppressed due to the integration, and thus, the Compton profile would be less affected by this.

D. Einstein-like approximation for phonon contribution

Let us consider a model where the electron orbital on a site fluctuates with noise characterized by a Gaussian distribution. Then the modified orbital is given as

$$\widetilde{\Phi}_{\nu\mathbf{k}}(\mathbf{r}) = \int d\mathbf{x}\Phi_{\nu\mathbf{k}}(\mathbf{r}+\mathbf{x})f(\mathbf{x}), \tag{17}$$

where $f(\mathbf{x}) = (2\pi\alpha)^{-3/2}\exp(-\frac{x^2}{2\alpha})$, ν is the band index, and $\Phi_{\nu\mathbf{k}}(\mathbf{r})$ is the original wave function. Taking the Fourier transform and making a change of variable, $\mathbf{r}' = \mathbf{r}+\mathbf{x}$, we get

$$\begin{aligned}\widetilde{\Phi}_{\nu\mathbf{k}} &= \int d\mathbf{r}\widetilde{\Phi}_{\nu\mathbf{k}}(\mathbf{r})e^{-i\mathbf{k}\cdot\mathbf{r}} \\ &= \int d\mathbf{r}'\Phi_{\nu\mathbf{k}}(\mathbf{r}')e^{-i\mathbf{k}\cdot\mathbf{r}'}\int d\mathbf{x}f(\mathbf{x})e^{i\mathbf{k}\cdot\mathbf{x}} \\ &= \Phi_{\nu\mathbf{k}}e^{-\alpha k^2/2}.\end{aligned} \tag{18}$$

Therefore, the modified momentum distribution will be $n(\mathbf{k})e^{-\alpha k^2}$ since $\sum_\nu|\widetilde{\Phi}_{\nu\mathbf{k}}|^2 = \sum_\nu|\Phi_{\nu\mathbf{k}}e^{-\alpha k^2/2}|^2 = \sum_\nu|\Phi_{\nu\mathbf{k}}|^2e^{-\alpha k^2} = n(\mathbf{k})e^{-\alpha k^2}$. The sum over ν includes only occupied orbitals.

III. RESULTS AND DISCUSSION

As expected due to the prior success of QMC in VO_2, our results yield good agreement with the experimental Compton profile data [1]. For example, at $q = 0$ our values including the Hartree-Fock core contribution [84] are $10.456(4)ea_0^{-1}$ and $10.444(4)ea_0^{-1}$ for the R phase and $M1$ phase, respectively. For the $M1$ phase an experimental value of $10.102(22)ea_0^{-1}$ and a DFT–linear combination of atomic orbitals value of 9.761 are reported in Ref. [1], and in Ref. [26] a value of $10ea_0^{-1}$ was used for $J_R(0)$. However, in general a more accurate measure both experimentally and computationally is given by considering differences between the phases since, e.g., the core contributions and some experimental uncertainties will cancel. Considering the subtle changes across the transition in a scaled difference profile [26], i.e., $[J_R(q) - J_{M1}(q)]/J_R(0)\times 100\%$, we find only a good qualitative correspondence. This is shown in Fig. 2. The change in the scaled difference profile is very delicate; for all q the scaled difference in $J(q)$ between the $M1$ and R phases remains below 0.2%. The related experimental data in Fig. 2 are multiplied

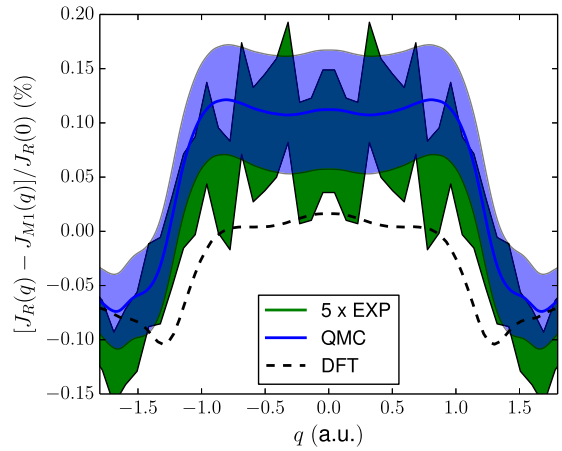

FIG. 2. Scaled Compton profile difference across the phase transition. Experimental data [26] in green have been multiplied by 5 in order to account for the quantitative difference in the scaled difference profile. Quantum Monte Carlo with 1σ statistical error is shown in blue (on top of the experiment), and DFT from this work (LDA+U with a DMC-optimized U value, $U = 3.5$ eV) is shown as a black dashed line. Here we concentrate on the region in which DFT, QMC, and the experiments have noticeable differences, i.e., the region of valence electron contributions.

by a factor of 5 (as in Ref. [26]) in order to obtain good quantitative correspondence in the scaled difference profile between theory and experiment. As argued by Ruotsalainen *et al.* [26], this effect is believed to derive from the electron-phonon coupling, which would indicate small, uneven changes in the Compton profile values for the high-temperature and low-temperature phases. The change would need only to be less than 0.1% in order to account for the observed quantitative difference. Using our simple Einstein solidlike picture, we derived an on-site approximation for the electron wave function influenced by nuclear motion. Within this harmonic model the momentum distribution would include an additional phonon-related term, i.e., $n(\mathbf{k}) \longrightarrow n(\mathbf{k})\exp(-\alpha k^2)$, in which α is the variance of a Gaussian distribution in position space. Already, $\alpha_R - \alpha_{M1} \approx 0.0001a_0^2$ would be enough to remove the quantitative discrepancy between theory and experiment. Therefore, a slight increase in the thermal motion and/or softening of phonon modes when going from the $M1$ to R phase is a likely explanation for the factor of 5 in the difference profile. The softening of the phonon modes has been reported, for example, in Ref. [22]. It should be pointed out that this simple model removes the quantitative discrepancy only for a limited range, i.e., roughly $|q| < 1.0a_0^{-1}$.

In Ref. [26] it was shown that DFT within LDA+U and LDA approaches results in negative scaled Compton profile differences for small momentum transfer values. In our previous study [8] we optimized the Hubbard U of LDA+U with DMC. This procedure finds the optimal U value for the trial wave function within our fixed-node DMC approach that provides a rigorous upper bound for the total energy. Interestingly, we find that this procedure also results in improved agreement with experiments already at the DFT level by increasing the small momentum values of $\Delta J(q)/J_R(0)$ close to zero on the positive side. The agreement is further enhanced

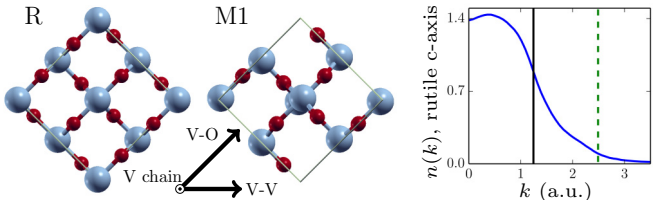

FIG. 3. Supercell crystal structures of R and $M1$ phases specifying directions used in the analysis. The vanadium chain direction (rutile c axis in general) is out of plane. Subtle structural changes can be seen, e.g., the misalignment of the V atoms along the chain direction (zigzag "chain"). On the right we show the momentum distribution in the R phase along the vanadium chain direction. The statistical error bars are smaller than the linewidth. Vertical lines are estimates for the Fermi momentum k_F and $2k_F$ obtained from the angular-averaged "isotropic" momentum distribution.

by the more accurate correlation description provided by QMC, as shown in Fig. 2, where we show the challenging region. Outside the limits of this region all the curves are in very good agreement with each other.

In Fig. 3 we show our supercell crystal structures of the two phases and define the general directions used in the analysis of the momentum distributions. There the vanadium chain direction (or rutile c axis) is out of plane. Subtle structural changes can be seen, e.g., the misalignment of the V atoms along the chain direction in the $M1$ phase. There the vanadium atoms are arranged in a "zigzag"-type chain structure. Raising the temperature above the transition temperature will lead to a perfectly aligned chain along the V chain direction and complementary changes also in the V-V and V-O directions shown in Fig. 3. In addition, in the R phase along the V chain direction the vanadium atoms are evenly spaced, in contrast to the $M1$ phase, which increases the electron hopping amplitude along the chain [85].

On the right in Fig. 3 we show the momentum distribution in the metallic R phase along the vanadium chain direction. The statistical error bars are smaller than the width of the line, and the vertical lines are estimates of the Fermi momentum k_F and $2k_F$. Due to the absence of a clear discontinuity the Fermi momentum is estimated by the position of the minimum value in the first derivative of the angular-averaged momentum distribution. Importantly, this absence of a discontinuity indicates non-Fermi liquid behavior in the metallic rutile phase. Our result agrees with recent experimental findings [15], where the violation of the Wiedemann-Franz law was attributed to the formation of a strongly correlated, incoherent non-Fermi liquid. There the charge and heat were considered to be transported by distinct diffusive modes instead of long-lived quasiparticles. For a more detailed view on the possible source for this non-Fermi liquid behavior, we will next look into the directional characteristics of the momentum distribution in both phases and also across the transition.

In Fig. 4 we present DMC anisotropies in the momentum distribution in two different planes for both phases: the R phase and $M1$ phase are on a plane given by the rutile c axis (V chain direction) and the V-O direction in Figs. 4(a) and 4(b), respectively, whereas in Figs. 4(c) and 4(d) the R phase and $M1$ phase are on a plane given by the rutile c axis and the V-V direction indicated in Fig. 3. As a measure

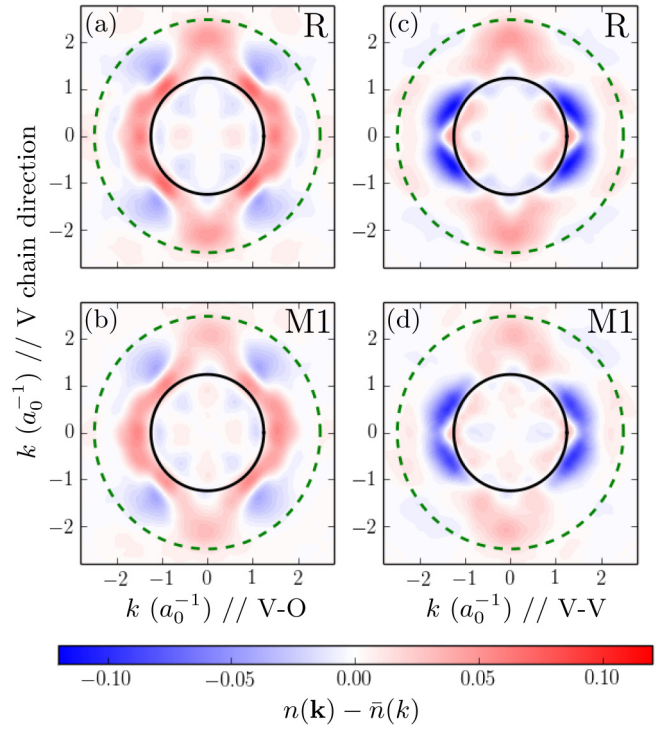

FIG. 4. Anisotropies of the momentum distribution on two different planes. Plane 1: V chain direction (y axis) versus V-O direction (x axis) for (a) the R phase and (b) $M1$ phase. Plane 2: V chain direction (y axis) versus V-V direction (x axis) for (c) the R phase and (d) $M1$ phase. The smaller circle is an estimate of Fermi momentum k_F from the angular-averaged "isotropic" momentum distribution, and the larger circle is at $\sim 2k_F$.

of anisotropy we use the difference $n(\mathbf{k}) - \bar{n}(k)$, where $\bar{n}(k)$ is the angular-averaged momentum distribution. Comparing Figs. 4(a) and 4(b) we can see that the anisotropy is, in general, stronger in the R phase than in the $M1$ phase. This is rather counterintuitive considering the differences in crystal structures of the two phases; on the other hand, it is indicative of the effects of electron-electron interactions and electron correlations. Interestingly, based on quasiparticle wave functions the GW approach would indicate an electronically more isotropic R phase [13]. The Seebeck coefficient measurements of Ref. [27], however, agree with our observations of noticeably larger anisotropy in the R phase. The negative Seebeck values indicate that the dominant current carriers are electrons, but according to the simple model in Ref. [27], the anisotropy can be explained if more than one type of current carrier with different and anisotropic mobilities is present. However, as we see here, the large anisotropy is present already at the electronic level. The most noticeable differences in Figs. 4(a) and 4(b) are manifested along the c axis where the R phase appears isotropic up to $\sim k_F$, with a large anisotropic contribution at $\sim 2k_F$. In the V chain–V-V plane [Figs. 4(c) and 4(d)], the anisotropy is stronger along the "x" axis than in Figs. 4(a) and 4(b). Moreover, apart from the chain direction the anisotropies between the planes are of different sign close to the Fermi momentum. Expressed in a percentage measure similar to that of the Compton profile difference in Fig. 2, i.e., $[n - \bar{n}]/n_{\max} \times 100\%$, these anisotropies would yield values

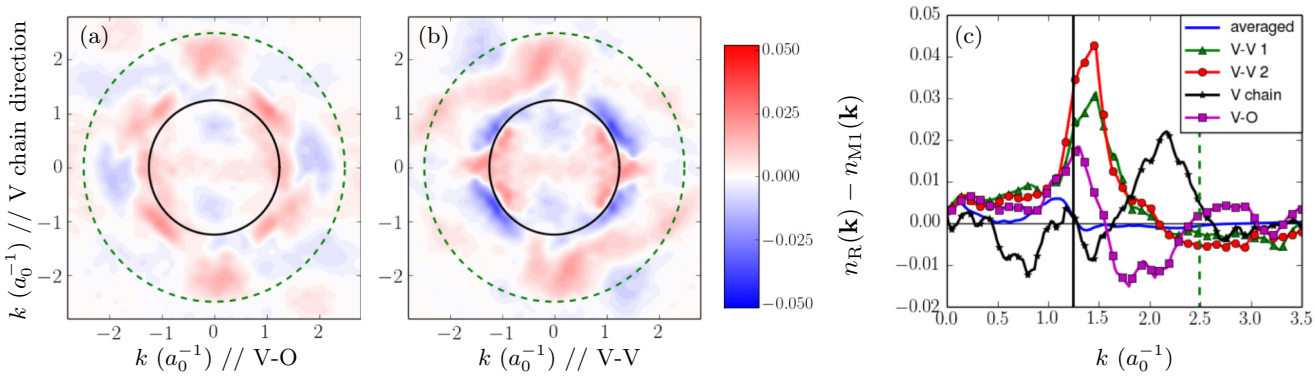

FIG. 5. Difference in the momentum distribution across the phase transition on the same two planes as in Fig. 4: (a) V chain direction (y axis) versus V-O direction (x axis) and (b) V chain direction (y axis) versus V-V direction (x axis). The smaller circle is an estimate of Fermi momentum k_F from the angular-averaged isotropic momentum distribution, and the larger circle is at $\sim 2k_F$. In (c) the differences are given in four different directions and also for the angular-averaged momentum distributions. In (c) the V-V 1 direction corresponds to the x axis of (b), and V-V 2 is the direction straight up in Fig. 3, i.e., perpendicular to V-V 1.

up to $\sim$10%, which is significantly larger than the anisotropies in the Compton profile (<1.2% in Ref. [1]). Therefore, the anisotropies should give a clear signal in the experimental momentum distributions obtainable, e.g., through triple-differential cross-section measurements [31].

In Figs. 5(a) and 5(b) we consider the momentum distribution across the phase transition on the same two planes as in Fig. 4, whereas in Fig. 5(c) we show the difference along a few different directions as well as for the angular average. In Figs. 5(a) and 5(b) we see that below $k < k_F$ the momentum distribution (and therefore also the average electron momentum) along the x axis is enhanced, while along the vanadium chain direction (y axis) it is suppressed. Moreover, characteristics similar to those of the anisotropies can be seen at $2k_F$ along the V-chain direction; however, in Fig. 5(b) this is more spread out than in Fig. 4. The $\sim 2k_F$ character across the phase transition can be related to an increase in Friedel oscillations as a result of backscattering, in which an electron is scattered to the opposite side of the Fermi surface; this is typical, e.g., in the context of Luttinger liquid theory, spin density waves, and electron-phonon scattering [34,37–39]. The spatial period for Friedel oscillations would, however, be rather small to observe, i.e., of the order of $\pi/k_F \approx 2.5a_0$, but its major contribution would be in the vanadium chain direction. In general, the $2k_F$ backscattering can lead to degradation of both the electrical and thermal currents and is thus a likely reason for the observed anomalously low electronic thermal conductivity found fairly recently for the R phase [15]. But where does this $2k_F$ character derive from, and why is it mainly observable in the V chain direction? In the Luttinger liquid model a short-range impurity will lead to Friedel oscillations that are scaled by a term including the interaction strength. Due to the absence of impurity atoms in our simulations the interactions between the rutile c axis and directions perpendicular to it are expected to induce impurities [86] resulting in the quasi-1D $\sim 2k_F$ character of these oscillations. In a rough picture this would be formed of linked one-dimensional chains, essentially comprising an anisotropic component of the broader three-dimensional electronic structure, where the links are responsible for the impurity effects. This picture is supported by the electron density considerations addressed below. The quasi-1D behavior was reported earlier based on GW calculations considering the role of crystal local-field and excitonic effects [14], where the quasi-1D nature was shown to influence the optical properties of VO_2. The increased probabilities and the anisotropies observed here also support the experimental results for the Seebeck coefficients [27], which indicate an $\sim$9% smaller conductivity along the rutile c axis compared to the directions perpendicular to it. Importantly, Fig. 5 describes the electron momentum transfer in the MIT, thus also providing new complementary knowledge of phase transition.

To this end, Fig. 5 shows a considerable anisotropic shift in the momentum distribution function and a change in its character: along the V-V1, V-V2, and also V-O directions there is a shift of weight towards momenta slightly larger than k_F, consistent with the formation of a more metallicklike Fermi surface in these directions. In contrast, the momentum distribution along the V-chain axis depletes weight from below k_F and adds considerable weight out towards $2k_F$. This is indicative of both a large "smearing" of the momentum distribution function and Friedel oscillations at $2k_F$, both consistent with a non-Fermi liquid-like behavior along the V-chain axis. In Fig. 6 we plot electron density isoconcentration surfaces: the R phase in Figs. 6(a) and 6(b) and the $M1$ phase in Figs. 6(c) and 6(d). Clear 1D chainlike isoconcentration surfaces along the V-chain directions are observed with real-space oscillations corresponding to the momentum distribution peak near $2k_F$. These plots are also consistent with 1D non-Fermi liquid-like behavior along the V-chain direction. These observations lead to the following picture: in the insulating $M1$ phase, dimerization along the V chains driven by correlations prevents the formation of metallicity, and the system is insulating. As the MIT is approached from the $M1$ phase, correlation energy diminishes (relative to other energies), allowing the formation of a Fermi surface. However, a remnant of strong correlations along the V-chain axis leads to non-Fermi liquid-like behavior along this direction. It is also insightful to consider the MIT from the metallic side. Strong correlations along the V-chain axis prevent the

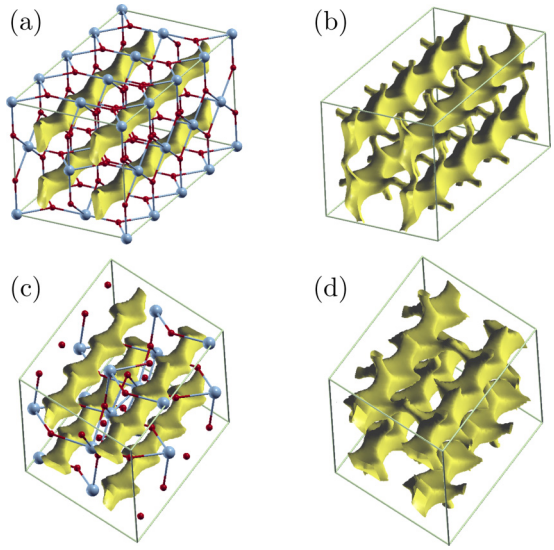

FIG. 6. Electron density isosurfaces (atomic units, e/a_0^3): (a) R phase with an isovalue of 0.06, (b) R phase with an isovalue of 0.08, (c) $M1$ phase with an isovalue of 0.06, and (d) $M1$ phase with an isovalue of 0.08. Quantum Monte Carlo electron densities are from the Materials Data Facility related to Ref. [8]. For clarity the atoms are not shown in (b) and (d). These figures were made with XCRYSDEN [87,88].

formation of a clear Fermi surface in those directions, leading to non-Fermi liquid-like behavior along the V chains. As the MIT is approached from the R phase, correlation strengths increase, leading to dimerization and the insulating $M1$ phase. In other words, the MIT is driven primarily by electronic correlations, not by structural instabilities.

In the R phase the oscillations in the electron density for the 1D chains are identical, whereas in the M1 phase they are not. Actually, in the M1 phase a nearest-neighbor 1D chain has a phase shift of half the period, which changes the positions of the maxima and minima. Slightly increasing the isovalue, i.e., going from Fig. 6(a) to Fig. 6(b), we see a formation of "links" between the chains. In the R phase the number of these links is larger than in the $M1$ phase with the same isovalue. This is likely related to the enhancement of backscattering seen in the MIT and further supports the Luttinger picture of connected/linked 1D chains introduced earlier.

IV. CONCLUSIONS

In this study we used first-principles quantum Monte Carlo to obtain the momentum distribution and Compton profiles for the R and $M1$ phases of vanadium dioxide. Good qualitative agreement with the experimental data was shown for the Compton profile differences across the metal-insulator transition. The quantitative differences are considered to arise from electron-phonon coupling based on a simple theoretical model and experimental observations [26]. Analysis of the momentum distribution reveals the signature of the non-Fermi liquid character of the metallic R phase proposed by recent experiments [15]. Moreover, we observe that Friedel oscillations in the R phase are mainly confined to one dimension, which together with the observed $\sim 2k_F$ characteristics is reminiscent of a Luttinger liquid-type metal with impurities. These impurities could emerge as a consequence of the transverse dimensions. In addition, we believe that our findings provide an explanation for the experimentally observed anomalously low electronic thermal conductivity [15], as we observe backscattering characteristics within the momentum distribution.

The Department of Energy will provide public access to these results of federally sponsored research in accordance with the DOE Public Access Plan [89].

In addition, full simulation inputs and outputs for all QMC and DFT calculations performed in this work are available via the Materials Data Facility [90].

ACKNOWLEDGMENTS

We thank Ruotsalainen *et al.* [26] for providing the experimental data and D. Ceperley, Y. Yang, and A. Kogar for useful comments. This work was supported by the US Department of Energy, Office of Science, Basic Energy Sciences, Materials Sciences and Engineering Division, as part of the Computational Materials Sciences Program and Center for Predictive Simulation of Functional Materials. An award of computer time was provided by the Innovative and Novel Computational Impact on Theory and Experiment (INCITE) Program. This research used resources of the Argonne Leadership Computing Facility, which is a US Department of Energy Office of Science User Facility operated under Contract No. DE-AC02-06CH11357, and the resources of the Oak Ridge Leadership Computing Facility at the Oak Ridge National Laboratory, which is supported by the Office of Science of the US Department of Energy under Contract No. DE-AC05-00OR22725. ORNL is managed by UT-Battelle, LLC, under Contract No. DE-AC05-00OR22725 with the US Department of Energy. The United States Government retains and the publisher, by accepting the article for publication, acknowledges that the United States Government retains a non-exclusive, paid-up, irrevocable, worldwide license to publish or reproduce the published form of this manuscript, or allow others to do so, for United States Government purposes.

[1] M. Vashistha, D. R. Phalaswal, K. Kabra, R. Kumar, B. K. Sharma, and G. Sharma, Mater. Focus **5**, 517 (2016).
[2] M. Imada, A. Fujimori, and Y. Tokura, Rev. Mod. Phys. **70**, 1039 (1998).
[3] Z. Zhang, F. Zuo, C. Wan, A. Dutta, J. Kim, J. Rensberg, R. Nawrodt, H. H. Park, T. J. Larrabee, X. Guan, Y. Zhou, S. M. Prokes, C. Ronning, V. M. Shalaev, A. Boltasseva, M. A. Kats, and S. Ramanathan, Phys. Rev. Appl. **7**, 034008 (2017).
[4] A. Zylbersztejn and N. F. Mott, Phys. Rev. B **11**, 4383 (1975).
[5] V. Eyert, Ann. Phys. (Berlin, Ger.) **11**, 650 (2002).
[6] Z. Zhu and U. Schwingenschlögl, Phys. Rev. B **86**, 075149 (2012).

[7] R. Grau-Crespo, H. Wang, and U. Schwingenschlögl, Phys. Rev. B **86**, 081101 (2012).

[8] I. Kylänpää, J. Balachandran, P. Ganesh, O. Heinonen, P. R. C. Kent, and J. T. Krogel, Phys. Rev. Mater. **1**, 065408 (2017).

[9] H. Zheng and L. K. Wagner, Phys. Rev. Lett. **114**, 176401 (2015).

[10] S. Biermann, A. Poteryaev, A. I. Lichtenstein, and A. Georges, Phys. Rev. Lett. **94**, 026404 (2005).

[11] J. M. Tomczak, F. Aryasetiawan, and S. Biermann, Phys. Rev. B **78**, 115103 (2008).

[12] W. H. Brito, M. C. O. Aguiar, K. Haule, and G. Kotliar, Phys. Rev. Lett. **117**, 056402 (2016).

[13] M. Gatti, F. Bruneval, V. Olevano, and L. Reining, Phys. Rev. Lett. **99**, 266402 (2007).

[14] M. Gatti, F. Sottile, and L. Reining, Phys. Rev. B **91**, 195137 (2015).

[15] S. Lee, K. Hippalgaonkar, F. Yang, J. Hong, C. Ko, J. Suh, K. Liu, K. Wang, J. J. Urban, X. Zhang, C. Dames, S. A. Hartnoll, O. Delaire, and J. Wu, Science **355**, 371 (2017).

[16] Y. Chen, S. Zhang, F. Ke, C. Ko, S. Lee, K. Liu, B. Chen, J. W. Ager, R. Jeanloz, V. Eyert, and J. Wu, Nano Lett. **17**, 2512 (2017).

[17] D. Y. Lei, K. Appavoo, F. Ligmajer, Y. Sonnefraud, R. F. Haglund, and S. A. Maier, ACS Photonics **2**, 1306 (2015).

[18] W. A. Vitale, M. Tamagnone, N. Émond, B. L. Drogoff, S. Capdevila, A. Skrivervik, M. Chaker, J. R. Mosig, and A. M. Ionescu, Sci. Rep. **7**, 41546 (2017).

[19] W. A. Vitale, E. A. Casu, A. Biswas, T. Rosca, C. Alper, A. Krammer, G. V. Luong, Q.-T. Zhao, S. Mantl, A. Schüler, and A. M. Ionescu, Sci. Rep. **7**, 355 (2017).

[20] D. W. Ferrara, J. Nag, E. R. MacQuarrie, A. B. Kaye, and R. F. Haglund, Nano Lett. **13**, 4169 (2013).

[21] J. Holleman, M. M. Bishop, C. Garcia, J. S. R. Vellore Winfred, S. Lee, H. N. Lee, C. Beekman, E. Manousakis, and S. A. McGill, Phys. Rev. B **94**, 155129 (2016).

[22] J. D. Budai, J. Hong, M. E. Manley, E. D. Specht, C. W. Li, J. Z. Tischler, D. L. Abernathy, A. H. Said, B. M. Leu, L. A. Boatner, R. J. McQueeney, and O. Delaire, Nature (London) **515**, 535 (2014).

[23] F. J. Morin, Phys. Rev. Lett. **3**, 34 (1959).

[24] A. Tselev, I. A. Lukyanchuk, I. N. Ivanov, J. D. Budai, J. Z. Tischler, E. Strelcov, A. Kolmakov, and S. V. Kalinin, Nano Lett. **10**, 4409 (2010).

[25] M. A. Huber, M. Plankl, M. Eisele, R. E. Marvel, F. Sandner, T. Korn, C. Schüller, R. F. Haglund, R. Huber, and T. L. Cocker, Nano Lett. **16**, 1421 (2016).

[26] K. O. Ruotsalainen, J. Inkinen, T. Pylkkänen, T. Buslaps, M. Hakala, K. Hämäläinen, and S. Huotari, Eur. Phys. J. B **91**, 225 (2018).

[27] C. N. Berglund and H. J. Guggenheim, Phys. Rev. **185**, 1022 (1969).

[28] P. Lindner, Phys. Scr. **15**, 112 (1977).

[29] B. G. Williams, Phys. Scr. **15**, 92 (1977).

[30] M. J. Cooper, Rep. Prog. Phys. **48**, 415 (1985).

[31] F. Bell and J. R. Schneider, J. Phys.: Condens. Matter **13**, 7905 (2001).

[32] *Momentum Distributions*, edited by R. N. Silver and P. E. Sokol (Plenum, New York, 1989).

[33] F. Zambelli, L. Pitaevskii, D. M. Stamper-Kurn, and S. Stringari, Phys. Rev. A **61**, 063608 (2000).

[34] S. B. Dugdale, Phys. Scr. **91**, 053009 (2016).

[35] S. Huotari, J. A. Soininen, T. Pylkkänen, K. Hämäläinen, A. Issolah, A. Titov, J. McMinis, J. Kim, K. Esler, D. M. Ceperley, M. Holzmann, and V. Olevano, Phys. Rev. Lett. **105**, 086403 (2010).

[36] M. Holzmann, B. Bernu, C. Pierleoni, J. McMinis, D. M. Ceperley, V. Olevano, and L. Delle Site, Phys. Rev. Lett. **107**, 110402 (2011).

[37] K. Schönhammer, *Strong Interactions in Low Dimensions*, edited by D. Baeriswyl and L. Degiorgi (Springer, 2004), Vol. 25, pp. 93–136.

[38] S.-i. Tomonaga, Prog. Theor. Phys. **5**, 544 (1950).

[39] J. M. Luttinger, J. Math. Phys. **4**, 1154 (1963).

[40] N. Hiraoka and T. Nomura, Sci. Rep. **7**, 565 (2017).

[41] C. Filippi and D. M. Ceperley, Phys. Rev. B **59**, 7907 (1999).

[42] W. M. C. Foulkes, L. Mitas, R. J. Needs, and G. Rajagopal, Rev. Mod. Phys. **73**, 33 (2001).

[43] J. Kim, A. T. Baczewski, T. D. Beaudet, A. Benali, M. C. Bennett, M. A. Berrill, N. S. Blunt, E. J. L. Borda, M. Casula, D. M. Ceperley, S. Chiesa, B. K. Clark, R. C. Clay III, K. T. Delaney, M. Dewing, K. P. Esler, H. Hao, O. Heinonen, P. R. C. Kent, J. T. Krogel, I. Kylänpää, Y. W. Li, M. G. Lopez, Y. Luo, F. D. Malone, R. M. Martin, A. Mathuriya, J. McMinis, C. A. Melton, L. Mitas, M. A. Morales, E. Neuscamman, W. D. Parker, S. D. P. Flores, N. A. Romero, B. M. Rubenstein, J. A. R. Shea, H. Shin, L. Shulenburger, A. F. Tillack, J. P. Townsend, N. M. Tubman, B. V. D. Goetz, J. E. Vincent, D. C. Yang, Y. Yang, S. Zhang, and L. Zhao, J. Phys.: Condens. Matter **30**, 195901 (2018).

[44] N. M. Tubman, I. Kylänpää, S. Hammes-Schiffer, and D. M. Ceperley, Phys. Rev. A **90**, 042507 (2014).

[45] Y. Yang, I. Kylänpää, N. M. Tubman, J. T. Krogel, S. Hammes-Schiffer, and D. M. Ceperley, J. Chem. Phys. **143**, 124308 (2015).

[46] C. J. Umrigar, M. P. Nightingale, and K. J. Runge, J. Chem. Phys. **99**, 2865 (1993).

[47] J. B. Anderson, J. Chem. Phys. **63**, 1499 (1975).

[48] D. M. Ceperley and B. J. Alder, Phys. Rev. Lett. **45**, 566 (1980).

[49] L. K. Wagner and D. M. Ceperley, Rep. Prog. Phys. **79**, 094501 (2016).

[50] L. K. Wagner, J. Phys.: Condens. Matter **19**, 343201 (2007).

[51] J. Kolorenč and L. Mitas, Phys. Rev. Lett. **101**, 185502 (2008).

[52] L. Mitas and J. Kolorenč, Rev. Mineral. Geochem. **71**, 137 (2010).

[53] J. Kolorenč, S. Hu, and L. Mitas, Phys. Rev. B **82**, 115108 (2010).

[54] K. Foyevtsova, J. T. Krogel, J. Kim, P. R. C. Kent, E. Dagotto, and F. A. Reboredo, Phys. Rev. X **4**, 031003 (2014).

[55] L. K. Wagner and P. Abbamonte, Phys. Rev. B **90**, 125129 (2014).

[56] J. Yu, L. K. Wagner, and E. Ertekin, J. Chem. Phys. **143**, 224707 (2015).

[57] J. A. Schiller, L. K. Wagner, and E. Ertekin, Phys. Rev. B **92**, 235209 (2015).

[58] L. K. Wagner, Phys. Rev. B **92**, 161116 (2015).

[59] Y. Luo, A. Benali, L. Shulenburger, J. T. Krogel, O. Heinonen, and P. R. C. Kent, New J. Phys. **18**, 113049 (2016).

[60] J. A. Santana, J. T. Krogel, P. R. C. Kent, and F. A. Reboredo, J. Chem. Phys. **144**, 174707 (2016).

[61] A. Benali, L. Shulenburger, J. T. Krogel, X. Zhong, P. R. C. Kent, and O. Heinonen, Phys. Chem. Chem. Phys. **18**, 18323 (2016).
[62] K. Doblhoff-Dier, J. Meyer, P. E. Hoggan, G.-J. Kroes, and L. K. Wagner, J. Chem. Theory Comput. **12**, 2583 (2016).
[63] J. Trail, B. Monserrat, P. López Ríos, R. Maezono, and R. J. Needs, Phys. Rev. B **95**, 121108 (2017).
[64] J. Yu, L. K. Wagner, and E. Ertekin, Phys. Rev. B **95**, 075209 (2017).
[65] M. Holzmann, B. Bernu, and D. M. Ceperley, J. Phys.: Conf. Ser. **321**, 012020 (2011).
[66] J. Longo and P. Kierkegaard, Acta Chem. Scand. **24**, 420 (1970).
[67] M. Ghedira, H. Vincent, M. Marezio, and J. Launay, J. Solid State Chem. **22**, 423 (1977).
[68] M. Hellenbrandt, Crystallogr. Rev. **10**, 17 (2004).
[69] B. Blaiszik, K. Chard, J. Pruyne, R. Ananthakrishnan, S. Tuecke, and I. Foster, JOM **68**, 2045 (2016).
[70] P. Giannozzi, S. Baroni, N. Bonini, M. Calandra, R. Car, C. Cavazzoni, D. Ceresoli, G. L. Chiarotti, M. Cococcioni, I. Dabo, A. Dal Corso, S. de Gironcoli, S. Fabris, G. Fratesi, R. Gebauer, U. Gerstmann, C. Gougoussis, A. Kokalj, M. Lazzeri, L. Martin-Samos, N. Marzari, F. Mauri, R. Mazzarello, S. Paolini, A. Pasquarello, L. Paulatto, C. Sbraccia, S. Scandolo, G. Sclauzero, A. P. Seitsonen, A. Smogunov, P. Umari, and R. M. Wentzcovitch, J. Phys.: Condens. Matter **21**, 395502 (2009).
[71] J. Kim, K. P. Esler, J. McMinis, M. A. Morales, B. K. Clark, L. Shulenburger, and D. M. Ceperley, J. Phys.: Conf. Ser. **402**, 012008 (2012).
[72] C. Lin, F. H. Zong, and D. M. Ceperley, Phys. Rev. E **64**, 016702 (2001).
[73] J. C. Slater, Phys. Rev. **34**, 1293 (1929).
[74] R. Jastrow, Phys. Rev. **98**, 1479 (1955).
[75] N. D. Drummond, M. D. Towler, and R. J. Needs, Phys. Rev. B **70**, 235119 (2004).
[76] C. J. Umrigar, J. Toulouse, C. Filippi, S. Sorella, and R. G. Hennig, Phys. Rev. Lett. **98**, 110201 (2007).
[77] M. M. Hurley and P. A. Christiansen, J. Chem. Phys. **86**, 1069 (1987).
[78] L. Mitas, E. L. Shirley, and D. M. Ceperley, J. Chem. Phys. **95**, 3467 (1991).
[79] M. Casula, Phys. Rev. B **74**, 161102 (2006).
[80] C. J. Umrigar and C. Filippi, Phys. Rev. Lett. **94**, 150201 (2005).
[81] J. B. Anderson, J. Chem. Phys. **65**, 4121 (1976).
[82] G. Ortiz, D. M. Ceperley, and R. M. Martin, Phys. Rev. Lett. **71**, 2777 (1993).
[83] M. Casula, C. Filippi, and S. Sorella, Phys. Rev. Lett. **95**, 100201 (2005).
[84] F. Biggs, L. Mendelsohn, and J. Mann, At. Data Nucl. Data Tables **16**, 201 (1975).
[85] E. Caruthers and L. Kleinman, Phys. Rev. B **7**, 3760 (1973).
[86] C. L. Kane and M. P. A. Fisher, Phys. Rev. Lett. **76**, 3192 (1996).
[87] A. Kokalj, Comput. Mater. Sci. **28**, 155 (2003).
[88] A. Kokalj, J. Mol. Graphics Modell. **17**, 176 (1999).
[89] http://energy.gov/downloads/doe-public-access-plan.
[90] I. Kylanpaa, Y. Luo, O. Heinonen, P. Kent, and J. Krogel, Dataset for Compton profile of VO2 across the metal-insulator transition: evidence of a non-Fermi liquid metal, 2019, http://dx.doi.org/doi:10.18126/M28K90.